

Temperature-dependent spectroscopy and microchip laser operation of Nd:KGd(WO₄)₂

P. Loiko^{1,2}, S.J. Yoon³, J.M. Serres¹, X. Mateos^{1,4}, S.J. Beecher³, R.B. Birch⁵, V.G. Savitski⁵, A.J. Kemp⁵, K. Yumashev², U. Griebner⁴, V. Petrov⁴, M. Aguiló¹, F. Díaz¹ and J.I. Mackenzie^{3,*}

¹*Física i Cristal·lografia de Materials i Nanomaterials (FiCMA-FiCNA), Universitat Rovira i Virgili (URV), Campus Sescelades, c/ Marcel·lí Domingo, s/n., Tarragona, Spain E-43007*

²*Center for Optical Materials and Technologies, Belarusian National Technical University, 65/17 Nezavisimosti Ave., Minsk, Belarus 220013*

³*Optoelectronics Research Centre, University of Southampton, Highfield, Southampton SO171BJ, UK*

⁴*Max Born Institute for Nonlinear Optics and Short Pulse Spectroscopy, Max-Born-Str. 2a, Berlin, Germany D-12489*

⁵*Institute of Photonics, Dept. of Physics, University of Strathclyde, SUPA, Technology and Innovation Centre, 99 George Street, Glasgow, G1 1RD, UK*

*Corresponding author, e-mail: jim@orc.soton.ac.uk

Abstract High-resolution absorption and stimulated-emission cross-section spectra are presented for monoclinic Nd:KGd(WO₄)₂ (Nd:KGW) laser crystals in the temperature range 77-450 K. At room-temperature, the maximum stimulated emission cross-section is $\sigma_{SE} = 21.4 \times 10^{-20} \text{ cm}^2$ at 1067.3 nm, for light polarization $E \parallel N_m$. The lifetime of the ⁴F_{3/2} state of Nd³⁺ in KGW is practically temperature independent at $115 \pm 5 \mu\text{s}$. Measurement of the energy transfer upconversion parameter for a 3 at.% Nd:KGW crystal proved that this was significantly smaller than for alternative hosts, $\sim 2.5 \times 10^{-17} \text{ cm}^3/\text{s}$. When cut along the N_g optical indicatrix axis, the Nd:KGW crystal was configured as a microchip laser, generating $\sim 4 \text{ W}$ of continuous-wave output at 1067 nm with a slope efficiency of 61% under diode-pumping. Using a highly-doped (10 at.%) Nd:KGW crystal, the slope efficiency reached 71% and 74% when pumped with a laser diode and a Ti:Sapphire laser, respectively. The concept of an ultrathin (250 μm) Nd:KGW microchip laser sandwiched between two synthetic diamond heat-spreaders is demonstrated.

Keywords: double tungstate; neodymium; microchip laser; diamond; luminescence

1. Introduction

Monoclinic double tungstates, $KRE(WO_4)_2$, where RE stands for an optically passive rare-earth element like Gd, Y or Lu, are exceptionally suitable for doping with active rare-earth ions like Nd^{3+} , Yb^{3+} , Tm^{3+} or Ho^{3+} [1]. Such host-dopant combinations offer intense and broad absorption and emission bands with a strong polarization-anisotropy [2,3], high doping concentrations without significant luminescence quenching [4], and they are Raman-active [5]. The thermal conductivity of double tungstates (~ 3 W/mK) is three times higher than that of laser glasses [6]. As a result, medium-power but highly efficient continuous-wave (CW) [7,8], Q-switched [9,10] and mode-locked [11,12] double tungstate lasers utilizing various geometries of the active element (e.g., bulk, slab, thin-disk) have been reported to date.

The unique combination of attractive spectroscopic properties and high RE doping make the double tungstates very interesting for microchip lasers [13]. Such lasers consist of a gain medium and optionally a saturable absorber for Q-switching placed in a plano-plano laser cavity without air gaps. The compact, robust and low-loss design provides high laser efficiency [13]. However, the possibility to exploit the advantages of double tungstates in the microchip geometry was hampered for many years by the negative thermal lens of these materials [14] resulting mainly from negative thermo-optic coefficients [15]. Recently, a crystal orientation was determined that can provide access both to the high-gain laser polarizations and a positive thermal lens, independent of the active ion [8,16,17]. This orientation is realized by cutting along one of the principal axes of the optical indicatrix of these biaxial crystals (N_g -axis). As a result, highly-efficient Yb, Tm and Ho double tungstate microchip lasers were reported recently [18-20].

The implementation of a Nd-doped double tungstate microchip as active medium is of great interest as it can fully exploit the advantage of the 4-level laser medium, i.e. very low laser threshold in a low-loss microchip cavity resulting in high optical-to-optical laser efficiency. Among the double tungstates, $KGd(WO_4)_2$ (commonly shortened to KGW) is the best host for Nd^{3+} doping due to the similarity of the ionic radii of eight-fold oxygen-coordinated Gd^{3+} (1.053 Å) and Nd^{3+} (1.109 Å). Thus, doping up to 10 at.% Nd is possible, whilst it is limited to ~ 2 at.% for KYW and KLuW host crystals.

To date, studies of Nd:KGW have focused mainly on the development of efficient low-threshold lasers emitting at ~ 1 μm and 1.35 μm [21,22]. Nd:KGW is an interesting laser crystal for several other reasons. First, the main laser transition of Nd^{3+} ions in KGW ($^4F_{3/2} \rightarrow ^4I_{11/2}$) generates a wavelength (~ 1067 nm) that is slightly longer than that of Nd:YAG and Nd:YVO₄ (~ 1064 nm). If frequency doubled, this corresponds to a green emission at 533.6 nm, which is exceptionally suitable for pumping of visible (deep-red, ~ 702 nm) Eu^{3+} lasers [23]. In addition, it can be used for in-band pumping of green upconversion Ho^{3+} lasers (to the $^5F_4+^5S_2$ state). Secondly, KGW is a well-known Raman-active material with an intense vibrational mode at 901 cm^{-1} that enabled the operation of a CW Nd:KGW Raman laser [5]. The combination of the $^4F_{3/2} \rightarrow ^4I_{11/2}$ emission with self-Raman conversion and second-harmonic generation can produce yellow light sources (at ~ 590 nm). In addition, Raman conversion of the $^4F_{3/2} \rightarrow ^4I_{13/2}$ emission (~ 1351 nm) can lead to the generation in the eye-safe spectral region at ~ 1540 nm. Finally, in comparison with Nd:YAG and Nd:YVO₄ crystals, Nd:KGW has much broader absorption bands at 808 nm [24]. The latter, together with the higher achievable Nd^{3+} concentrations mentioned above, makes Nd:KGW lasers almost insensitive to temperature drift of the pump diode wavelength – a feature, successfully exploited in a ChemCam laser system, developed for space applications [25].

In the present work, we aim to exploit the spectroscopic and thermo-optic features of Nd:KGW for microchip laser operation. Detailed reconsideration of spectroscopic properties of Nd:KGW is motivated by a discrepancy in the results reported to date [26,27], as well as the lack of information with regard to temperature-dependence of the absorption and stimulated-emission (SE) cross-sections for low and elevated temperatures. The former are of practical importance for cryogenic lasers, a concept that can mitigate the main drawback of Nd:KGW (i.e., strong thermo-optic aberrations). The latter are useful for understanding the effects of strongly localized heating produced by the dissipation of pump power in Nd:KGW lasers. Moreover, the dependence of SE cross-sections on temperature has been utilized for significant energy scaling in Q-switched Nd:YVO₄ microchip formats [28], simply by increasing the temperature of the laser gain material. With a lower SE cross-section and similar lifetime, Nd:KGW has the potential for even higher pulse energies than Nd:YVO₄ using compact Q-switched microchip laser cavities at elevated temperatures of the gain material. Therefore, detailed information on the temperature-dependence of the SE cross-sections in Nd:KGW is essential for the development of compact Q-switched lasers based on this crystal. Finally, we present the first CW laser action of ultrathin (250 μm) Nd:KGW crystal sandwiched between two diamond heat-spreaders as an initial step towards realization of such microchip lasers.

2. Optical spectroscopy

For the spectroscopic studies, we used 1 mm-thick 3 and 4 at.% Nd:KGW crystals ($N_{Nd} = 1.9$ and 2.5×10^{20} at/cm³, respectively). The 3 at.% crystal was cut along the N_g -axis of the optical indicatrix (the orientation that is of interest for microchip laser operation) thus providing access to the two other principal light polarization states, $E \parallel N_m$ and N_p . The second crystal was N_m -cut, providing access to $E \parallel N_g$ and N_p emission.

For the absorption measurements, undertaken with the 3 at.% sample, a broadband amplified spontaneous emission (ASE) source, a polarizer, and an optical spectrum analyzer (OSA) with 0.1 nm resolution were used. The experimental setup is shown in Fig. 1. Two different fiber-coupled (fiber diameter: 200 μm, N.A. = 0.22) light sources were employed. One of the sources was a diode laser with a nominal lasing wavelength of 805 nm (LIMO60-F200-DL808); however, operation below the laser threshold delivered ~100 mW of ASE covering the wavelength range 780-840 nm. The second source, an 870 nm high-power light-emitting diode (LED) (JET-870-05 Roithner Lasertechnik) produced ~10 mW of output power at the exit facet with an emission spectrum covering 850-910 nm. Both probe light sources were coupled into a measurement fiber. The exit facet of the latter was fixed in position and imaged in the sample with three times magnification. The light transmitted through the sample was subsequently re-imaged into the endface of a fiber patch cable and sent to an OSA (ANDO AQ6317B). A broadband cube polarizer was used to isolate the respective principal optical polarization of interest, $\parallel N_m$ and $\parallel N_p$. Figure 2 illustrates emission spectra for both ASE sources measured before and after the Nd:KGW crystal.

Absorption spectra for the Nd:KGW crystal corresponding to the $^4I_{9/2} \rightarrow ^4F_{5/2}$ and $^4I_{9/2} \rightarrow ^4F_{3/2}$ transitions, measured at room temperature (300 K), are shown in Fig. 3(a) for the studied polarization states, $E \parallel N_m$ and N_p . For both transitions, a significant anisotropy is detected with the larger absorption cross-sections (σ_{abs}) corresponding to $E \parallel N_m$. For the $^4I_{9/2} \rightarrow ^4F_{5/2}$ transition and light polarization $E \parallel N_m$, the absorption band contains an intense peak with a maximum $\sigma_{abs}(m) = 29 \times 10^{-20}$ cm² at 810.5 nm and a full width at half maximum (FWHM) of 1.7 nm. For $E \parallel N_p$, this band contains two peaks of similar intensity centered at 806.2 and 810.5 nm with their

maxima $\sigma_{\text{abs}}(p) \sim 6 \times 10^{-20} \text{ cm}^2$. For the ${}^4I_{9/2} \rightarrow {}^4F_{3/2}$ transition and both polarizations, the absorption band contains two intense peaks centered at 875.7 nm (FWHM = 2.3 nm) and 883.8 nm (FWHM = 1.6 nm). The second peak dominates and the corresponding values for the maximum absorption cross-sections are $\sigma_{\text{abs}}(m) = 8.8$ and $\sigma_{\text{abs}}(p) = 4.8 \times 10^{-20} \text{ cm}^2$.

As the strongest absorption in Nd:KGW corresponds to the polarization state $E \parallel N_m$, we have performed temperature-dependent measurements for this polarization alone. However, for the ${}^4I_{9/2} \rightarrow {}^4F_{5/2}$ transition at low temperatures, we were limited by the very strong absorbance of the 1 mm-thick crystal, so the measurements for this transition were only conducted for the 300–450 K range, Fig. 3(b). At the maximum elevated temperature tested (450 K), the $\sigma_{\text{abs}}(m)$ peak decreased by a factor of 1.8, as compared with its room-temperature value, while the FWHM bandwidth slightly increased to 2.7 nm.

For the ${}^4I_{9/2} \rightarrow {}^4F_{3/2}$ transition, limitation of strong absorption can be overcome by fitting the spectral shape of the local peaks with a Lorentzian function, as can be expected for Raman broadened transitions [29]. This allowed us to reconstruct the shape of the absorption band for 77–450 K as shown in Fig. 3(c). The local peak centered at 883.8 nm is of main interest for in-band pumping of Nd:KGW. At 77 K, the peak $\sigma_{\text{abs}}(m)$ is estimated to be $62 \times 10^{-20} \text{ cm}^2$ (FWHM = 0.3 nm) and at 450 K, $\sigma_{\text{abs}}(m)$ is reduced to $4.7 \times 10^{-20} \text{ cm}^2$ (FWHM = 3.2 nm). In Fig. 3(d), we plot the peak $\sigma_{\text{abs}}(m)$ values at 810.5 nm (${}^4I_{9/2} \rightarrow {}^4F_{5/2}$) and 883.8 nm (${}^4I_{9/2} \rightarrow {}^4F_{3/2}$) versus temperature. The values of σ_{abs} determined in the present study at room temperature are consistent with the results published by Chen et al. [26].

To determine the SE cross section (σ_{SE}), we used the Füchtbauer-Ladenburg (F-L) method for anisotropic crystals [30] in combination with the McCumber or Reciprocity Method (RM) [31] for the transition terminating in the ground-state manifold, ${}^4I_{9/2}$. It was of particular importance to determine the real emission cross section spectrum around the zero-phonon line at 884 nm because of the strong reabsorption at the shorter wavelengths of the ${}^4F_{3/2} \rightarrow {}^4I_{9/2}$ transition. As KGW is a biaxial crystal this approach requires the measurement of the shape of the luminescence spectrum $W(\lambda)$ for the three polarization states aligned to each of the principal axes ($i = p, m$ and g), and the lifetime of the emitting level, τ . The emission cross section spectrum for each respective polarization state is obtained via the F-L equation:

$$\sigma_{\text{SE}}^i(\lambda) = \frac{\lambda^5 \eta_q}{8\pi n_i^2 \tau c} \frac{3\beta(JJ')W_i(\lambda)}{\sum_{i=p,m,g} \int \lambda W_i(\lambda) d\lambda}, \quad (1)$$

where n_i is the refractive index for the i -th polarization, c is the speed of light, $\beta(JJ')$ is the luminescence branching ratio for each transition ${}^4F_{3/2} (J) \rightarrow {}^4I_{9/2}$, ${}^4I_{11/2}$ and ${}^4I_{13/2} (J')$ and η_q is the fluorescence quantum efficiency.

The luminescence measurement set-up is depicted in Fig. 4. It allowed the temperature dependence measurements. The Nd:KGW crystal was pumped using the same unpolarized 805 nm fiber-coupled diode laser, now operated as a laser with an output power of ~ 2 W. A two-times magnified image of the fiber facet provided an irradiance of $< 1.5 \text{ kW/cm}^2$ at the sample to prevent ground state depletion. Although the saturation intensity at the 810 nm peak for $E \parallel N_m$ is 7.4 kW/cm^2 , for our pump wavelength at ~ 805 nm this value was substantially higher. Polarized emission spectra were taken over the spectral range of 850–1450 nm with a resolution of 0.1 nm, corresponding to the transitions from the upper metastable manifold, ${}^4F_{3/2}$, to the lowest three excited-state manifolds ${}^4I_{13/2}$, ${}^4I_{11/2}$ and ${}^4I_{9/2}$. The luminescence decay of the Nd^{3+} ions from the ${}^4F_{3/2}$ state was measured under quasi-CW excitation at 810 nm by a Ti:Sapphire laser. The pulse

duration of the chopped beam was a few ms. Luminescence was detected using a focusing lens, a photodiode and a digital oscilloscope (MSO6104A, Agilent Technology Inc.).

The characteristic decay time for the luminescence of Nd³⁺ ions in KGW from the ⁴F_{3/2} state amounted to 115±5 μs, characterized with a Ti:Sapphire laser pump, modulated by an optical chopper producing 1 ms pulses with a measured fall time (90 – 10%) of 10 μs. The lifetime of this state, was nearly independent of the temperature in the 77-450 K range. This value agrees well with the one reported in [26] at room temperature, 117 μs. Based on the radiative lifetime for the ⁴F_{3/2} manifold (111 μs [26]), we conclude that the fluorescence quantum efficiency for this manifold is close to unity.

SE cross-section spectra for Nd:KGW corresponding to the ⁴F_{3/2}→⁴I_{13/2}, ⁴I_{11/2} and ⁴I_{9/2} transitions measured at 300 K are shown in Fig. 5 for polarizations $E \parallel N_p$, N_m , and N_g . As previously reported the ⁴F_{3/2} → ⁴I_{11/2} transition has a strong anisotropy in emission, with the highest σ_{SE} values observed for $E \parallel N_m$. In particular, we obtained a maximum stimulated emission cross-section for $E \parallel N_m$, $\sigma_{SE}(m) = 21.4 \times 10^{-20} \text{ cm}^2$ at 1067.3 nm, in contrast for $E \parallel N_p$ at 1069.0 nm it is only $\sigma_{SE}(p) = 9.5 \times 10^{-20} \text{ cm}^2$. Additionally, for $E \parallel N_p$, a second intense peak is observed at 1056.0 nm, which could be favorable for dual-wavelength laser operation. We studied the temperature-dependence (77-450 K) of the SE cross-section spectra for the ⁴F_{3/2}→⁴I_{11/2} transition for the polarization, $E \parallel N_m$, which is of interest for various laser applications. These measurements were undertaken using the 3 at.% N_g -cut crystal and the branching ratios $\beta_i(JJ')$ and emission intensity scaling factors of Eq. (1) were assumed constant across this temperature range. The results are presented in Fig. 6(a,b). When the temperature is raised from 77 K to 450 K, the maximum $\sigma_{SE}(m)$ decreases from 61×10^{-20} to $16.8 \times 10^{-20} \text{ cm}^2$ at 1067.3 nm. The width of the most intense emission peak corresponding to the ⁴F_{3/2}→⁴I_{11/2} transition does not change significantly with increasing temperature, whilst at low temperatures it is split into two components centered at 1067.3 and 1069.2 nm corresponding to transitions to the two lowest ⁴I_{11/2} Stark levels [32]. In Fig. 6(c) we plotted the peak $\sigma_{SE}(m)$ values at 1067.3 nm versus temperature.

For the ⁴F_{3/2}→⁴I_{9/2} transition, strong absorption around the zero-phonon line alters the shape of the measured fluorescence spectrum, which directly impacts the determination of the SE cross section spectra through Eq. (1). To obtain a clearer picture of the ⁴F_{3/2} → ⁴I_{9/2} SE spectrum, we have utilized the RM method. Following this approach we obtain maxima at 883.8 nm of $\sigma_{SE}(m) = 13.8 \times 10^{-20} \text{ cm}^2$, $\sigma_{SE}(p) = 7.5 \times 10^{-20} \text{ cm}^2$, and $\sigma_{SE}(g) = 3.0 \times 10^{-20} \text{ cm}^2$.

For the ⁴F_{3/2}→⁴I_{13/2} transition, the SE cross-sections for the polarizations $E \parallel N_m$ and N_g are quite close, $6.4 \times 10^{-20} \text{ cm}^2$ and $5.7 \times 10^{-20} \text{ cm}^2$ at 1351.3 nm, respectively. The values of σ_{SE} determined in the present study at room temperature are consistent with the emission spectra presented by Moncorge et al. [27].

Energy transfer upconversion (ETU) is an important effect influencing the depopulation in the upper laser level of Nd³⁺ under high pump intensities. Macroscopic ETU parameters can be determined by measuring the transmission of the pump beam through the sample. For high pump intensities, comparable to the saturation intensity, the ground state is depopulated and the pump transmission normally increases [33]. However, ETU works against this process depopulating the excited state thus decreasing its lifetime, which is equivalent to an increase in the saturation intensity, consequently, counteracting pump bleaching. To determine the ETU parameter (W_{ETU}), we used a Z-scan setup as described in [34]. The excitation beam from a Ti:Sapphire laser was mechanically chopped to provide several ms-long pulses. It was focused using a 300 mm lens mounted on an electronically-controlled translation stage to change the

beam size in the static crystal. During the scan, the intensity change of the transmitted pump was measured with a power meter (13PEM100, Melles Griot Inc.). The pump-laser beam size along the Z-scan path was separately measured using a beam profiler (Nanoscan II, OPHIR Inc.), giving a beam waist of $\sim 20 \mu\text{m}$. To fit the measured Z-scan curves, a simple two-level rate equation model was applied [34].

We made Z-scan measurements on a 1 mm-thick N_g -cut Nd:KGW crystal for two light polarizations, $E \parallel N_p$ and N_m , for which we only include the data for $E \parallel N_p$, as shown in Fig. 7. For $E \parallel N_m$ pump light and the wavelength tuned to the absorption peak, we observed a non-saturating dependence of the transmitted pump on pulse duration. The latter is indicated by other factors affecting the absorption efficiency, such as temperature. The ETU parameter deduced from these measurements was $W_{\text{ETU}} = 2.5 \times 10^{-17} \text{ cm}^3/\text{s}$ ($E \parallel N_p$) with a confidence level of $\pm 50\%$ as the response was not fitting the simple theoretical curves precisely. For cross checking, we conducted a similar experiment using a N_m -cut 4 at.% Nd:KGW crystal thus accessing $E \parallel N_g$ and $E \parallel N_p$ polarizations which yielded $W_{\text{ETU}} = 3.0$ and $1.5 \times 10^{-17} \text{ cm}^3/\text{s}$, respectively. As a result Nd:KGW can provide advantages in terms of reduced ETU when compared with other popular crystal hosts. As an example, in Nd:YAG with 1.1 at.% Nd doping, the ETU parameter amounted to $W_{\text{ETU}} = 7.5 \times 10^{-17} \text{ cm}^3/\text{s}$, and it seems to increase nearly linear with the doping concentration [35]. Figure 7 confirms that the model used does not provide precise fitting of the measured Z-scan curves. This discrepancy is attributed to additional energy decay pathways, e.g. excited state absorption and energy migration. Further studies to identify the de-excitation processes of the upper laser level are required but go beyond the scope of the current work.

3. Microchip laser operation

For the laser experiments, two Nd:KGW crystals with different concentrations of Nd^{3+} ions (3 at.% and 10 at.%) were used. Both crystals were cut for light propagation along the N_g -axis of the optical indicatrix (N_g -cut). The thicknesses of these two crystals were 3.0 and 0.8 mm, respectively. The $3.0 \times 3.0 \text{ mm}^2$ crystal faces spanned by the N_m and N_p axes were polished to laser quality and remained uncoated. The crystals were mounted in a Cu-holder providing cooling from all four lateral sides and Indium foil ensured the thermal contact. The holder was water-cooled down to $14 \text{ }^\circ\text{C}$.

The plano-plano cavity of the microchip laser consisted of a pump mirror (PM) antireflection (AR) coated for $0.78\text{--}0.98 \mu\text{m}$ and high-reflection (HR) coated for $1.02\text{--}1.23 \mu\text{m}$, and an output coupler (OC) providing transmittances $T_{\text{OC}} = 1, 5$ or 10% at the laser wavelength. Both mirrors were attached directly to the polished crystal faces without air gaps keeping the cavity length at $3.0/0.8 \text{ mm}$, the geometrical length of the Nd:KGW sample. As pump source, we used an AlGaAs fiber coupled laser diode (fiber core diameter: $200 \mu\text{m}$; numerical aperture N.A.: 0.22) emitting at $\sim 803 \text{ nm}$. This wavelength is out of the main absorption peak of Nd^{3+} ions in order to provide less localized pump absorption. The unpolarized pump radiation was collimated and focused into the crystal using a lens assembly (1:1 imaging ratio, 30 mm focal length) resulting in a pump spot radius w_p in the crystal of $\sim 100 \mu\text{m}$. The confocal parameter for the pump beam was $2z_R = 3.6 \text{ mm}$. No pump bleaching of the crystal absorption was observed. The measured absorption in the crystal was nearly independent of the pump level at $\sim 54\%$ and 72% for 3 at.% and 10 at.% doped crystals, respectively.

The selection of N_g -cut crystals for microchip experiments is due to the positive sign of the thermal lens for this orientation of Nd:KGW. This is shown in Fig. 8(a) where the optical power of the thermal lens D is plotted versus the absorbed pump power P_{abs} , see details in [36]. The

slope of this dependence is called sensitivity factor, $M = dD/dP_{\text{abs}}$. For Nd:KGW, the M -factors are different for rays lying in the orthogonal planes containing the N_m and N_p -axes, namely $M(m) = 2.4$ and $M(p) = 2.2 \text{ m}^{-1}/\text{W}$, respectively (as measured at 1067 nm for laser polarization $E \parallel N_m$ and the pump spot radius $w_p = 180 \text{ }\mu\text{m}$). The closeness of these values is usually expressed in terms of the degree of astigmatism $S = \Delta M/M$. The latter is only $\sim 8\%$ for N_g -cut Nd:KGW, leading to a near-circular profile of the laser beam. The above mentioned thermo-optic features (i.e., positive and nearly spherical thermal lens) make N_g -cut crystals ideal for microchip laser operation.

For all Nd:KGW microchip lasers investigated, their emission was linearly polarized ($E \parallel N_m$), naturally selected by the anisotropy of the gain, Fig. 5(a). First the 3 at.% Nd:KGW crystal was investigated and the use of $T_{\text{OC}} = 10\%$ corresponded to the best laser performance, Fig. 8(b). The maximum output power was 4.02 W at 1067 nm corresponding to a slope efficiency $\eta = 61\%$ with respect to absorbed pump power. The threshold was as low as 120 mW and the optical-to-optical efficiency was thus almost 60%. The input-output dependence for the Nd:KGW microchip laser was linear; however, we limited the range of studied pump powers to $P_{\text{abs}} < 7 \text{ W}$ to avoid stress fracture of the crystal. For $T_{\text{OC}} = 5\%$ and 1% , the slope efficiency of the laser dropped to 52% and 50%, respectively. For $T_{\text{OC}} = 1\%$, the laser threshold was $\sim 50 \text{ mW}$. The achieved results are comparable to those reported previously for a Nd:KGW conical-refraction laser [37] that generated 3.3 W with a slope efficiency of 74%. In contrast, our set-up is very compact and does not require a precise crystal orientation along its optical axis.

The output beam of the microchip laser was nearly circular as expected from the thermal lens properties corresponding to TEM₀₀ mode up to the maximum studied pump power. However, the $M^2_{x,y}$ factor ($x = p, y = m$) increased slightly from ~ 1.05 (near the threshold) to ~ 1.3 (for $P_{\text{abs}} > 6 \text{ W}$). The increase of the M^2 factor, as well as the slightly lower value of η as compared with the theoretical limit ($\sim 75\%$), is attributed mainly to the mode-matching conditions. For the considered pump spot size ($w_p = 100 \text{ }\mu\text{m}$), the sensitivity factors of the thermal lens, which are inversely proportional to the square of w_p , were $M = 7.6$ and $7.0 \text{ m}^{-1}/\text{W}$ for the directions of N_m and N_p -axes, respectively. Thus, the calculated radius of the TEM₀₀ laser mode in the crystal decreases from 70 to $55 \pm 5 \text{ }\mu\text{m}$ within the studied pump range.

Next we studied the 10 at.% Nd:KGW microchip laser. As with the 3 at.% Nd:KGW the 10% OC provided the best output performance, see Fig. 9(a). The calculated radius of the laser mode in the crystal was $\sim 60 \pm 5 \text{ }\mu\text{m}$. The microchip laser generated 1.05 W with the slope efficiency of 71% and an optical-to-optical efficiency of 62%. The output mode was TEM₀₀ with $M^2_{x,y} < 1.1$. The higher value of η as compared with 3 at.% Nd:KGW microchip is attributed to a better mode-matching. Because of the shorter crystal length the change of the pump mode radius along the beam path in the crystal was smaller. The laser threshold was at $P_{\text{abs}} = 150 \text{ mW}$. It should be noted that the output dependence for the 10 at.% Nd:KGW microchip was linear. However, operation at $P_{\text{abs}} > 2 \text{ W}$, was risky, mainly due to highly localized heat loading in the crystal and low efficiency of its side-cooling which may lead to stress fracture of the crystal.

An alternative way to improve the slope efficiency of the Nd:KGW microchip laser is pumping with a smaller beam waist. To verify this approach, we have studied the performance of the 10 at.% Nd:KGW sample under Ti:Sapphire laser pumping. The polarization of the $\sim 805 \text{ nm}$ pump beam was adjusted to be parallel to the N_m -axis of the Nd:KGW crystal. The pump was focused to a spot with a radius of $\sim 55 \pm 5 \text{ }\mu\text{m}$. 52% of the pump radiation was absorbed in the crystal. For $T_{\text{OC}} = 10\%$, the laser generated 341 mW of output power with a maximum slope efficiency of 74% which is very close to the value estimated from the quantum defect, 75.7%,

see Fig. 9(b). The laser threshold was at 52 mW and the optical-to-optical efficiency amounted to 67%. For $T_{OC} = 5\%$ and 1% , the slope efficiency was 70% and 64%, respectively.

We believe that further power scaling of highly-doped Nd:KGW microchip lasers is in principle possible, by substantial reduction of the thickness of the crystal together with cooling of one or both of the faces in order to reduce the probability of stress fracture. Besides, thinner crystals are essential for decreasing the overall length of the microchip cavity, opening the prospects for sub-ns laser pulse generation in Q-switched microchip lasers [38].

To prove the practical potential of very thin crystals for microchip lasers, we prepared 250 μm -thick plate with an aperture of $5 \times 5 \text{ mm}^2$ from a N_g -cut 3 at.% Nd:KGW crystal. This plate was polished from both sides and capillary-bonded between two synthetic diamonds (sandwich configuration). The non-contacted side of diamond heat-spreader #1 was AR-coated at the pump (808 nm) and laser (1067 nm) wavelength and the contacted side of diamond heat-spreader #2 was HR-coated for 0.8-1.1 μm thus serving as a HR mirror. The composite sample was mounted in brass holder chilled to 10°C via water cooling. The flat OC had a transmittance $T_{OC} = 2.4\%$ at the laser wavelength. It was positioned as close as possible to diamond heat-spreader #1 with a small air gap. The total cavity length was $\sim 2 \text{ mm}$. A 10 W fiber-coupled (core diameter: 200 μm) AlGaAs laser diode at 808 nm was used as pump source. The pump was collimated and focused to $\sim 150 \mu\text{m}$ spot radius into the crystal through the OC with a lens assembly. The calculated radius of the TEM_{00} mode in the crystal was $\sim 60 \pm 5 \mu\text{m}$. To separate the pump and laser beams, a dichroic mirror was inserted between the collimating and focusing lenses, oriented at 45° with respect to the pump beam. The scheme of the Nd:KGW / diamond microchip laser is shown in Fig. 10(a).

The Nd:KGW/diamond microchip laser delivered a maximum output power of 906 mW at 1067 nm in N_m polarization corresponding to a slope efficiency of 33%, Fig. 10(b). This value was mainly limited by poor mode-matching for pump and laser modes. The laser threshold was at 660 mW of absorbed pump power and the optical-to-optical efficiency was 24%. Power scaling of this laser was mainly limited by de-bonding of the sandwich structure. Improvements in the bonding and optimization of the coatings should significantly improve performance of this laser.

4. Conclusion

We report on a comprehensive temperature-dependent study of polarized absorption of monoclinic Nd:KGW crystals (within the $^4I_{9/2} \rightarrow ^4F_{3/2}$ and $^4I_{9/2} \rightarrow ^4F_{5/2}$ bands interesting for its pumping), as well as its stimulated-emission related to the transitions from the metastable $^4F_{3/2}$ manifold. ETU is estimated for Nd:KGW, yielding lower W_{ETU} values than Nd:YAG. At room-temperature, the maximum stimulated-emission cross-sections are $13.8 \times 10^{-20} \text{ cm}^2$ at 883.8 nm ($^4F_{3/2} \rightarrow ^4I_{9/2}$ transition), $21.4 \times 10^{-20} \text{ cm}^2$ at 1067.3 nm ($^4F_{3/2} \rightarrow ^4I_{11/2}$) and $6.4 \times 10^{-20} \text{ cm}^2$ at 1351.3 nm ($^4F_{3/2} \rightarrow ^4I_{13/2}$) for light polarization $E \parallel N_m$. The unique combination of highly polarized absorption and SE cross-sections, high possible Nd^{3+} doping level and a positive thermal lens is utilized to demonstrate multi-watt Nd:KGW microchip lasers with slope efficiency $>60\%$. The concept of composite 250 μm thick Nd:KGW/diamond laser is proposed. This first demonstration proves the potential of very thin Nd:KGW crystals bonded to diamond heat-spreader for future improvement of monolithic Q-switched microchip lasers. The data on temperature-dependent values of the SE cross-section in Nd:KGW also opens a new route towards energy scaling of Q-switched microchip lasers based on this crystal, which will be a subject of future research.

Acknowledgements

This work was supported by the Spanish Government under projects, MAT2013-47395-C4-4-R and TEC2014-55948-R, and by the Generalitat de Catalunya under project 2014SGR1358. F.D. acknowledges additional support through the ICREA academia award 2010ICREA-02 for excellence in research. This work is part of a project that has received funding from the European Union's Horizon 2020 research and innovation programme under the Marie Skłodowska-Curie grant agreement No 657630. S.J. Yoon would like to thank PSK Inc. (Korea) for financial support via a PhD scholarship. Funding support is acknowledged from the UK Engineering and Physical Sciences Research Council (EPSRC) through the grant EP/J008052/1, the European Research Council (grant number 278389), Fraunhofer UK Research Ltd., and the Royal Academy of Engineering, (data for the work undertaken as part of this funding as per Research Data Management policy can be found at DOI:[10.5258/SOTON/386964](https://doi.org/10.5258/SOTON/386964)).

References

1. V. Petrov, M.C. Pujol, X. Mateos, O. Silvestre, S. Rivier, M. Aguiló, R.M. Solé, J. Liu, U. Griebner, F. Díaz, *Laser & Photon. Rev.* 1 (2007) 179–212.
2. N.V. Kuleshov, A.A. Lagatsky, V.G. Shcherbitsky, V.P. Mikhailov, E. Heumann, T. Jensen, A. Dening, G. Huber, *Appl. Phys. B* 64 (1997) 409–413.
3. O. Silvestre, M. C. Pujol, M. Rico, F. Güell, M. Aguiló, F. Díaz, *Appl. Phys. B* 87 (2007) 707–716.
4. M. C. Pujol, M. A. Bursukova, F. Guell, X. Mateos, R. Sole, Jna. Gavalda, M. Aguiló, J. Massons, F. Diaz, P. Klopp, U. Griebner, V. Petrov, *Phys. Rev. B* 65 (2002) 165121-1–11.
5. A. A. Demidovich, A. S. Grabtchikov, V. A. Lisinetskii, V. N. Burakevich, V. A. Orlovich, W. Kiefer, *Opt. Lett.* 30 (2005) 1701–1703.
6. O. Silvestre, J. Grau, M.C. Pujol, J. Massons, M. Aguiló, F. Díaz, M.T. Borowiec, A. Szewczyk, M.U. Gutowska, M. Massot, A. Salazar, V. Petrov, *Opt. Express* 16 (2008) 5022–5034.
7. X. Mateos, V. Petrov, J. Liu, M. C. Pujol, U. Griebner, M. Aguiló, F. Díaz, M. Galan, G. Viera, *IEEE J. Quantum Electron.* 42 (2006) 1008–1015.
8. P.A. Loiko, V.E. Kisel, N.V. Kondratuk, K.V. Yumashev, N.V. Kuleshov, A.A. Pavlyuk, *Opt. Mater.* 35 (2013) 582–585.
9. J. Liu, V. Petrov, H. Zhang, and J. Wang, *Appl. Phys. B* 88 (2007) 527–530.
10. V.E. Kisel, A.S. Rudenkov, N.V. Kuleshov, A.A. Pavlyuk, *Opt. Lett.* 39 (2014) 3038–3041.
11. U. Griebner, S. Rivier, V. Petrov, M. Zorn, G. Erbert, M. Weyers, X. Mateos, M. Aguiló, J. Massons, F. Diaz, *Opt. Express* 13 (2005) 3465–3470.
12. S. Pekarek, C. Fiebig, M. C. Stumpf, A. E. H. Oehler, K. Paschke, G. Erbert, T. Sudmeyer, U. Keller, *Opt. Express* 18 (2010) 16320–16326.
13. J. J. Zayhowski, *Opt. Mater.* 11 (1999) 255–267.
14. P. A. Loiko, K. V. Yumashev, N. V. Kuleshov, V. G. Savitski, S. Calvez, D. Burns, A. A. Pavlyuk, *Opt. Express* 17 (2009) 23536–23543.
15. S. Biswal, S.P. O'Connor, S.R. Bowman, *Appl. Opt.* 44 (2005) 3093–3097.
16. F. Hoos, S. Li, T.P. Meyrath, B. Braun, H. Giessen, *Opt. Express* 16 (2008) 6041–6049.
17. M.S. Gaponenko, P.A. Loiko, N.V. Gusakova, K.V. Yumashev, N.V. Kuleshov, A.A. Pavlyuk, *Appl. Phys. B* 108 (2012) 603–607.
18. M. Gaponenko, N. Kuleshov, T. Südmeyer, *Opt. Express* 22 (2014) 11578–11582.
19. J. M. Serres, X. Mateos, P. Loiko, K. Yumashev, N. Kuleshov, V. Petrov, U. Griebner, M. Aguiló, F. Díaz, *Opt. Lett.* 39 (2014) 4247–4250.
20. J. M. Serres, P. Loiko, X. Mateos, K. Yumashev, N. Kuleshov, V. Petrov, U. Griebner, M. Aguiló, F. Díaz, *Opt. Mater. Express* 5 (2015) 661–667.
21. A. A. Demidovich, A. P. Shkadarevich, M. B. Danailov, P. Apai, T. Gasmi, V. P. Gribkovskii, A. N. Kuzmin, G. I. Ryabtsev, L. E. Batay, *Appl. Phys. B* 67 (1998) 11–15.
22. G. Boulon, G. Metrat, N. Muhlstein, A. Brenier, M. R. Kokta, L. Kravchik, Y. Kalisky, *Opt. Mater.* 24 (2003) 377–383.
23. P.A. Loiko, V.I. Dashkevich, S.N. Bagaev, V.A. Orlovich, A.S. Yasukevich, K.V. Yumashev, N.V. Kuleshov, E.B. Dunina, A.A. Kornienko, S.M. Vatnik, A.A. Pavlyuk, *Laser Phys.* 23 (2013) 105811–1–7.
24. X. Gong, Y. Chen, Y. Lin, Z. Luo, and Y. Huang, *J. Opt. Soc. Am. B* 26 (2009) 259–266.
25. S. Maurice, R. C. Wiens, M. Saccoccio, B. Barraclough, O. Gasnault, O. Forni, et al., *Space Sci. Rev.* 170 (2012) 95–166.

26. Y. Chen, Y. Lin, X. Gong, Q. Tan, J. Zhuang, Z. Luo, and Y. Huang, *J. Lumin.* 126 (2007) 653-660.
27. R. Moncorge, B. Chambon, J.Y. Rivoire, N. Garnier, E. Descroix, P. Laporte, H. Guillet, S. Roy, J. Mareschal, D. Pelenc, J. Doury, P. Farge, *Opt. Mater.* 8 (1997) 109-119.
28. A. Kausas, T. Taira, "MW, mJ-high-brightness giant-pulse Nd:YVO₄ microchip laser by cross-section control," in proceedings of the Advanced Solid State Lasers conference, P. ATh3A.6, OSA Technical Digest, Berlin, Germany 2015.
29. M. Eichhorn, *Appl. Phys. B* 93 (2008) 269-316.
30. P. F. Moulton, *J. Opt. Soc. Am. B* 3 (1986) 125–133.
31. B.F. Aull, H.P. Jenssen, *IEEE J. Quantum Electron.* 18 (1982) 925–930.
32. A. A. Kaminskii, "Crystalline lasers: Physical Processes and Operating Schemes", CRC Press (1996) Chapter 2, 125.
33. C. Jacinto, D. N. Messias, A. A. Andrade, T. Catunda, *J. Opt. Soc. Am. B* 26 (2009) 1002-1007.
34. R.P. Yan, S. J. Yoon, S. J. Beecher, and J. I. Mackenzie, *IEEE J. Sel. Top. Quantum Electron.* 21 (2015) 329-336.
35. S.J. Yoon, R.P. Yan, S.J. Beecher, J.I. Mackenzie, *Opt. Mater. Express* 5 (2015) 926-931.
36. P.A. Loiko, V.G. Savitski, A. Kemp, A.A. Pavlyuk, N.V. Kuleshov, K.V. Yumashev, *Laser Phys. Lett.* 11 (2014) 055002-1–7.
37. A. Abdolvand, K. G. Wilcox, T. K. Kalkandjiev, E. U. Rafailov, *Opt. Express* 18 (2010) 2753-2759.
38. A. Steinmetz, D. Nodop, J. Limpert, R. Hohmuth, W. Richter, A. Tünnermann, *Appl. Phys. B.* 97 (2009) 317-320.

Figure Captions

Figure 1 Set-up for temperature-dependent absorption measurements: LD – laser diode, ASE – amplified spontaneous emission, OSA – optical spectrum analyzer.

Figure 2 Spectrum of the ASE laser source and transmitted spectrum after the Nd:KGW crystal (polarization $E \parallel N_m$) around the ${}^4I_{9/2} \rightarrow {}^4F_{5/2}$ (a) and ${}^4I_{9/2} \rightarrow {}^4F_{3/2}$ (b) transitions.

Figure 3 Absorption spectra of Nd:KGW crystal: (a) absorption bands related to the ${}^4I_{9/2} \rightarrow {}^4F_{5/2}$ and ${}^4I_{9/2} \rightarrow {}^4F_{3/2}$ transitions at 300 K for light polarizations $E \parallel N_m$ and $E \parallel N_p$; (b) ${}^4I_{9/2} \rightarrow {}^4F_{5/2}$ absorption at 300-450 K for $E \parallel N_m$; (c) ${}^4I_{9/2} \rightarrow {}^4F_{3/2}$ absorption at 77-450 K for $E \parallel N_m$; (d) peak absorption at 810.5 nm and 883.8 nm versus temperature.

Figure 4 Set-up for temperature-dependent emission measurements: LD – laser diode, OSA – optical spectrum analyzer.

Figure 5 Stimulated-emission cross-section spectra of Nd: KGW crystal for light polarizations $E \parallel N_p$ (a), N_m (b) and N_g (c) at room-temperature.

Figure 6 Temperature-dependence of stimulated-emission cross-sections of Nd:KGW crystal: ${}^4F_{3/2} \rightarrow {}^4I_{11/2}$ emission at 77-300 K (a) and at 300-450 K (b) for $E \parallel N_m$; (c) peak SE cross-section at 1067.3 nm for $E \parallel N_m$ versus temperature.

Figure 7 Open aperture Z-scan measurement: Nd:KGW crystal transmission at 810 nm versus Z-scan position relative to the focus for different crystal orientations and light polarizations, *symbols* are the experimental data, *solid-lines* are obtained from modeling to estimate W_{ETU} .

Figure 8 (a) Optical power of the thermal lens in N_g -cut Nd:KGW vs. absorbed pump power ($E \parallel N_m$); (b) laser characteristics for 3 mm-thick 3 at.% Nd:KGW microchip at 1067 nm, *inset* represents typical profiles of the output laser beam for $P_{abs} = 4$ W and 7 W ($T_{OC} = 10\%$).

Figure 9 Laser characteristics for 0.8-mm thick 10 at.% Nd:KGW microchip pumped with a laser diode (a), *inset*: typical profile of the laser beam for $P_{abs} = 1.8$ W, and Ti:Sapphire laser (b), *symbols* - experimental data, *lines* - fitting for the slope (η) calculation.

Figure 10 Composite Nd:KGW / diamond microchip laser: (a) Experimental scheme: LD – laser diode, CL and FL – collimating and focusing lens, M- dichroic mirror, OC – output coupler; (b) laser characteristics.

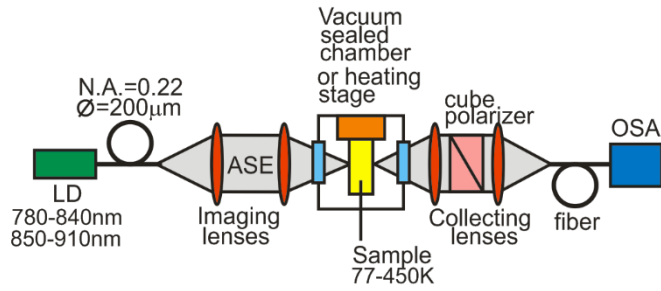


Figure 1 Set-up for temperature-dependent absorption measurements: LD – laser diode, ASE – amplified spontaneous emission, OSA – optical spectrum analyzer.

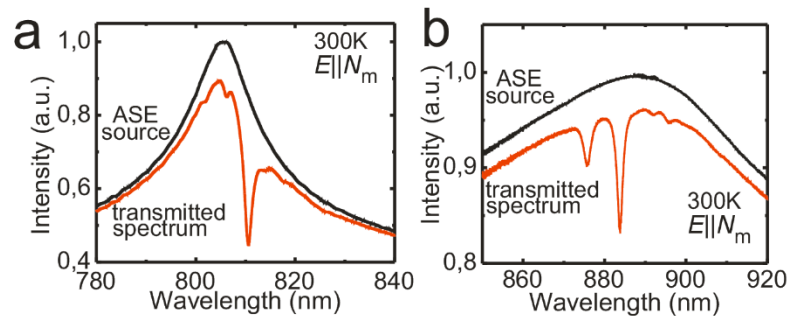


Figure 2 Spectrum of the ASE laser source and transmitted spectrum after the Nd:KGW crystal (polarization $E \parallel N_m$) around the ${}^4I_{9/2} \rightarrow {}^4F_{5/2}$ (a) and ${}^4I_{9/2} \rightarrow {}^4F_{3/2}$ (b) transitions.

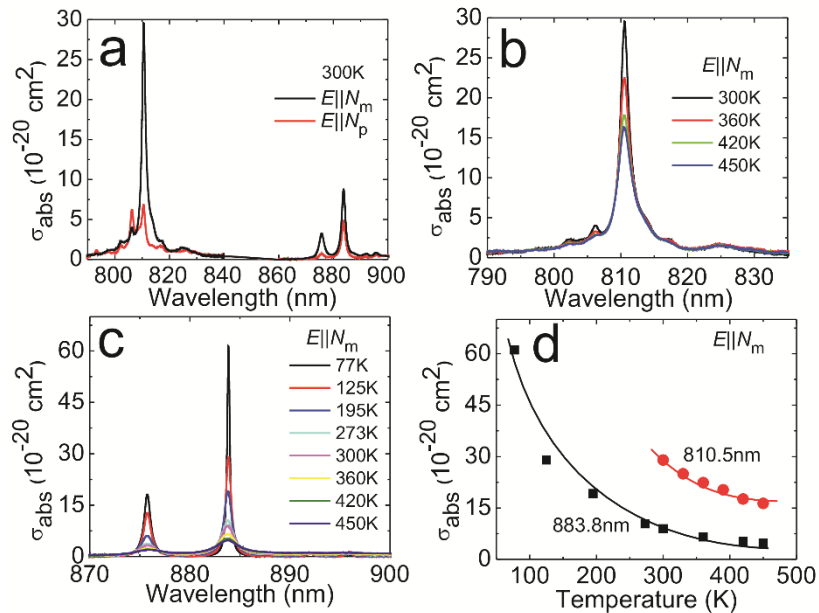


Figure 3 Absorption spectra of Nd:KGW crystal: (a) absorption bands related to the $4I_{9/2} \rightarrow 4F_{5/2}$ and $4I_{9/2} \rightarrow 4F_{3/2}$ transitions at 300 K for light polarizations $E \parallel N_m$ and $E \parallel N_p$; (b) $4I_{9/2} \rightarrow 4F_{5/2}$ absorption at 300-450 K for $E \parallel N_m$; (c) $4I_{9/2} \rightarrow 4F_{3/2}$ absorption at 77-450 K for $E \parallel N_m$; (d) peak absorption at 810.5 nm and 883.8 nm versus temperature.

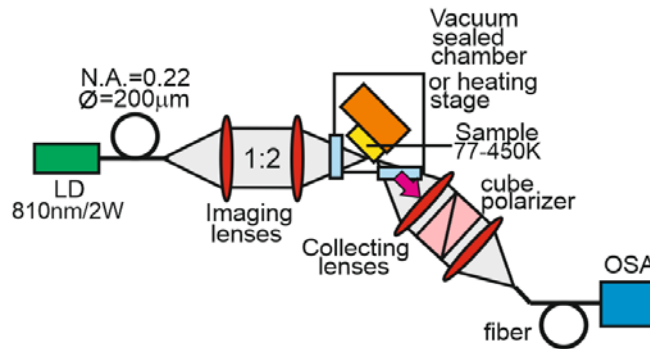


Figure 4 Set-up for temperature-dependent emission measurements: LD – laser diode, OSA – optical spectrum analyzer.

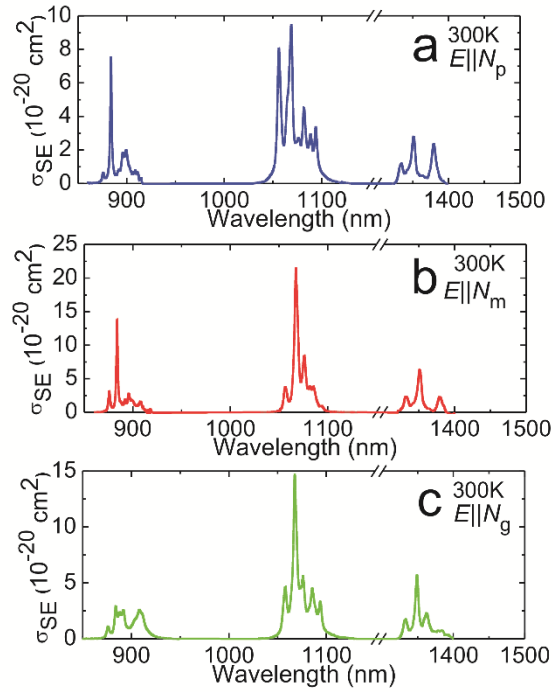


Figure 5 Stimulated-emission (SE) cross-section spectra of Nd:KGW crystal for light polarizations $E \parallel N_p$ (a), N_m (b) and N_g (c) at room-temperature.

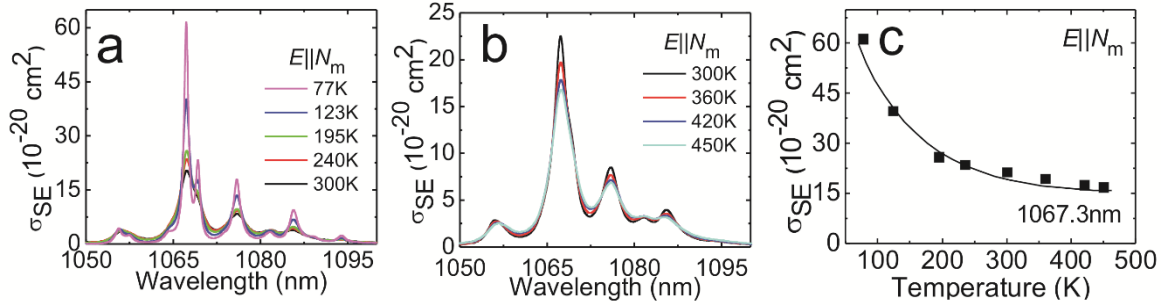


Figure 6 Temperature-dependence of stimulated-emission (SE) cross-sections of Nd:KGW crystal: ${}^4F_{3/2} \rightarrow {}^4I_{11/2}$ emission at 77-300 K (a) and at 300-450 K (b) for $E \parallel N_m$; (c) peak SE cross-section at 1067.3 nm for $E \parallel N_m$ versus temperature.

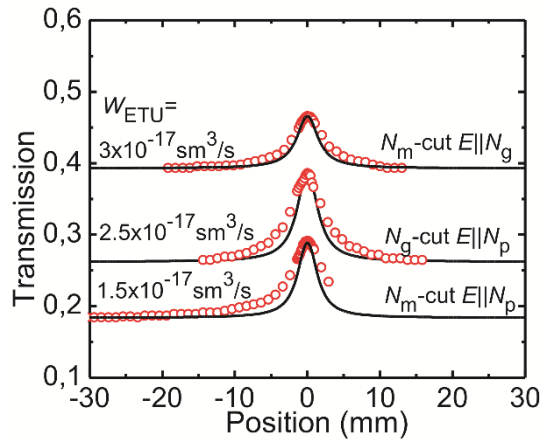


Figure 7 Open aperture Z-scan measurement: Nd:KGW crystal transmission at 810 nm versus Z-scan position relative to the focus for different crystal orientations and light polarizations, *symbols* are the experimental data, *solid-lines* are obtained from modeling to estimate W_{ETU} .

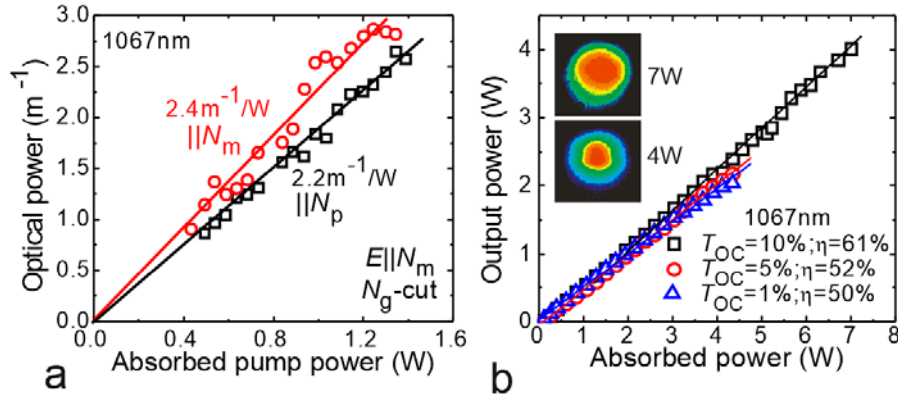


Figure 8 (a) Optical power of the thermal lens in N_g-cut Nd:KGW vs. absorbed pump power (E || N_m); (b) laser characteristics for 3 mm-thick 3 at.% Nd:KGW microchip at 1067 nm, *inset* represents typical profiles of the output laser beam for P_{abs} = 4 W and 7 W (T_{OC} = 10%).

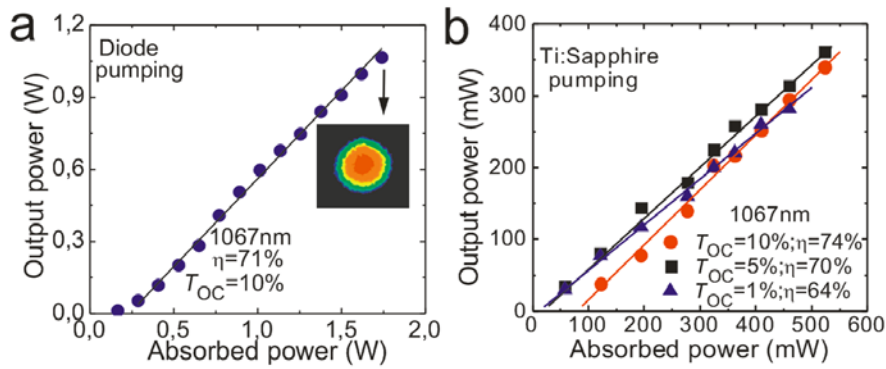


Figure 9 Laser characteristics for 0.8-mm thick 10 at.% Nd:KGW microchip pumped with a laser diode (a), *inset*: typical profile of the laser beam for P_{abs} = 1.8 W, and Ti:Sapphire laser (b), *symbols* - experimental data, *lines* - fitting for the slope (η) calculation.

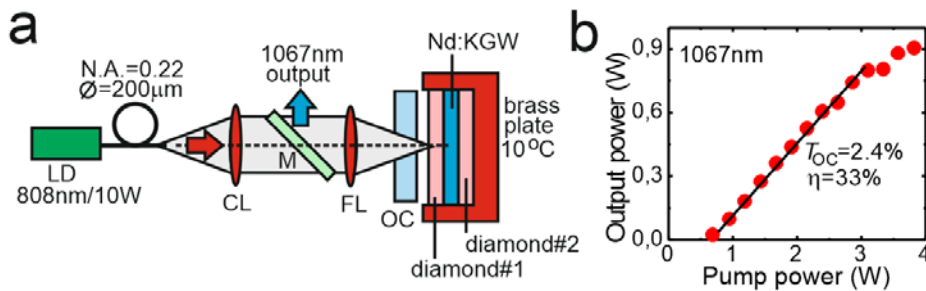


Figure 10 Composite Nd:KGW / diamond microchip laser: (a) Experimental scheme: LD – laser diode, CL and FL – collimating and focusing lens, M- dichroic mirror, OC – output coupler; (b) laser characteristics.